Chinese Journal of
POLYMER SCIENCE

RAPID COMMUNICATION

https://doi.org/10.1007/s10118-026-3647-0
Chinese J. Polym. Sci. **2026**, *44*, 2395–2402

Managing Interpenetration in 3D Covalent Organic Frameworks with Spatial-aromatic Building Blocks

Zhen-Yang Hu, Fu-Xiang Wen, Xiao-Yi Xu*, and Ning Huang*

State Key Laboratory of Silicon and Advanced Semiconductor Materials, Department of Polymer Science and Engineering, Zhejiang University, Hangzhou 310058, China

Electronic Supplementary Information

Abstract The regulation of interpenetration in three-dimensional covalent organic frameworks (3D COFs) poses a fundamental challenge while offering a powerful means to engineer their pore environments. In this study, we demonstrate that the geometry and electronic character of linear linkers are decisive for achieving such control. Using a rigid, sterically extended 6-connected trigonal prismatic amine building block, we synthesized an isoreticular pair of **acs**-topology 3D COFs to compare the influence of a fully aromatic linker. The resulting frameworks, tris(trimethylbis-4-aminophenylphenyl)benzene (TTAPB)- terephthalaldehyde (TPA)-COF and TTAPB-C,C-diformyl-*p*-carborane (DFCB)-COF, exhibited dramatically different degrees of interpenetration, 6-fold and 2-fold, respectively. This contrast originates directly from the linker core; the planar π-conjugated TPA promotes dense, multifold interpenetration, whereas the globular, electron-deficient carborane introduces steric and electronic constraints that strongly limit network replication. Consequently, the difference in the interpenetration dictates the distinct porosity and gas adsorption behavior. By elucidating the structure-determining roles of monomer geometry and electronic properties, this work establishes a rational design principle for programming interpenetration and porosity in 3D extended frameworks.

Keywords Covalent organic frameworks; Porous polymer; **acs** Topology; Gas adsorption

Citation: Hu, Z. Y.; Wen, F. X.; Xu, X. Y.; Huang, N. Managing interpenetration in 3D covalent organic frameworks with spatial-aromatic building blocks. *Chinese J. Polym. Sci.* **2026**, *44*, 2395–2402.

INTRODUCTION

Covalent organic frameworks (COFs) are an emerging class of porous crystalline materials that are constructed from organic building blocks linked by strong covalent bonds.[1–3] Precisely designed structures and versatile functionalities have attracted broad interest in materials science and chemistry.[4–6] To achieve permanent porosity, such crystalline frameworks must adopt robust architectures that resist structural collapse. However, in three-dimensional (3D) COFs, pore formation is often accompanied by interpenetration, that is, the orderly entanglement of two or more identical yet independent networks within the same crystal.[7–9] While interpenetration can enhance the thermodynamic stability of the overall framework, it simultaneously reduces the porosity, void space, and surface area, thereby directly affecting the functional performance. Thus, the degree of interpenetration establishes a critical balance between structural stability and accessible pore volume, with significant implications for applications such as gas adsorption,[10–13] molecular separation,[14–17] optoelectronics,[18–21] heterogeneous catalysis,[22–26] and drug delivery.[27–30] Nevertheless, achieving precise and predictable control over interpenetration remains a fundamental and persistent challenge in the design of functional 3D COFs.

Since the first report of an interpenetrated 3D COF (COF-300) by Yaghi *et al.* in 2009, only approximately 50 such structures have been documented to date.[31–34] Efforts to control interpenetration have largely focused on engineering molecular building blocks, primarily through two strategies: modulating linker length and tuning substituent groups. Although extending the linker can theoretically increase the intrinsic pore size of a single network, the accompanying increase in the free volume often thermodynamically favors higher-order interpenetration, a trend clearly observed in several **dia**-topology COFs.[35,36] Conversely, introducing bulky substituents, such as methyl, methoxy, or alkyl chains, can sterically hinder close network packing, thereby suppressing interpenetration.[37,38] However, these approaches have largely relied on modifying conventional planar π-conjugated aromatics, such as benzene or biphenyl. Consequently, the impact of fundamentally altering the spatial geometry and electronic nature of the monomer core on the interpenetration behavior of 3D COFs remains poorly understood.

Icosahedral carboranes ($C_2B_{10}H_{12}$) represent a distinct class

* Corresponding authors, E-mail: xxyzsq@zju.edu.cn (X.Y.X.)
E-mail: nhuang@zju.edu.cn (N.H.)
Special Topic: Porous Polymers
Received January 30, 2026; Accepted March 9, 2026; Published online June 3, 2026

of molecular clusters that depart fundamentally from classical benzenoid aromatics due to their three-dimensional geometry and three-dimensional aromaticity.[39–44] Previous work from our group has demonstrated that carborane-based monomers can serve as viable building blocks for constructing highly crystalline and porous 3D COFs.[45] To extend this line of inquiry and to examine how the inherent spatial and electronic properties of a monomer dictate interpenetration across different network topologies, we selected the **acs** topology as a structural platform, which is based on a six-connected trigonal prismatic node. Within this system, we synthesized two isoreticular 3D COFs from linear aldehyde linkers of identical length, but with diametrically opposed core units: planar benzene and globular carborane. Structural analysis revealed a striking contrast: the benzene-based framework adopts a 6-fold interpenetrated network, whereas its carborane-based analog exhibits only 2-fold interpenetration. To investigate how this engineered difference in interpenetration influences the pore microenvironment, we employed CO_2, CH_4, and N_2 as molecular probes with distinct sizes, polarities, and quadrupole moments. This work not only presents the first study of interpenetration in **acs**-type 3D COFs but also demonstrates how monomer geometry and aromaticity can direct the degree of interpenetration, offering a rational design strategy for porosity control in 3D COFs with diverse topologies.

EXPERIMENTAL

The experimental sections are detailed in the electronic supplementary information (ESI).

RESULTS AND DISCUSSION

In this study, we designed a novel, rigid, and sterically extended 6-connected trigonal prismatic amine building block, designated TTAPB, and employed it to construct 3D COFs with **acs** topology using terephthalaldehyde (TPA) and *C*,*C*-diformyl-*p*-carborane (DFCB) as linear linkers. This paired synthetic approach not only provides a rigid, highly interconnected, and well-defined framework but also establishes a controlled platform to directly isolate and evaluate how the spatial geometry and electronic nature of the linker core govern the resulting interpenetration architecture.[46,47] Two isoreticular COFs, denoted TTAPB-DFCB-COF and TTAPB-TPA-COF, were successfully synthesized (Fig. 1). Both materials were prepared *via* Schiff base condensation catalyzed by 6 mol/L aqueous acetic acid in a sealed Pyrex tube using a dioxane/mesitylene mixed solvent at 120 °C for 72 h. The resulting products were collected by centrifugation and thoroughly purified *via* Soxhlet extraction, yielding TTAPB-DFCB-COF and TTAPB-TPA-COF as white and light-yellow powders in 75% and 83% yield, respectively. Structural modeling confirmed that both frameworks adopted a three-dimensional **acs** topology, each featuring well-defined one-dimensional channels with an estimated pore diameter of about 1 nm.

The chemical composition and physical properties of the COFs were characterized using a comprehensive suite of analytical techniques. The FTIR spectra showed new stretching vibration peaks at 1656 cm^{-1} for TTAPB-DFCB-COF and 1596

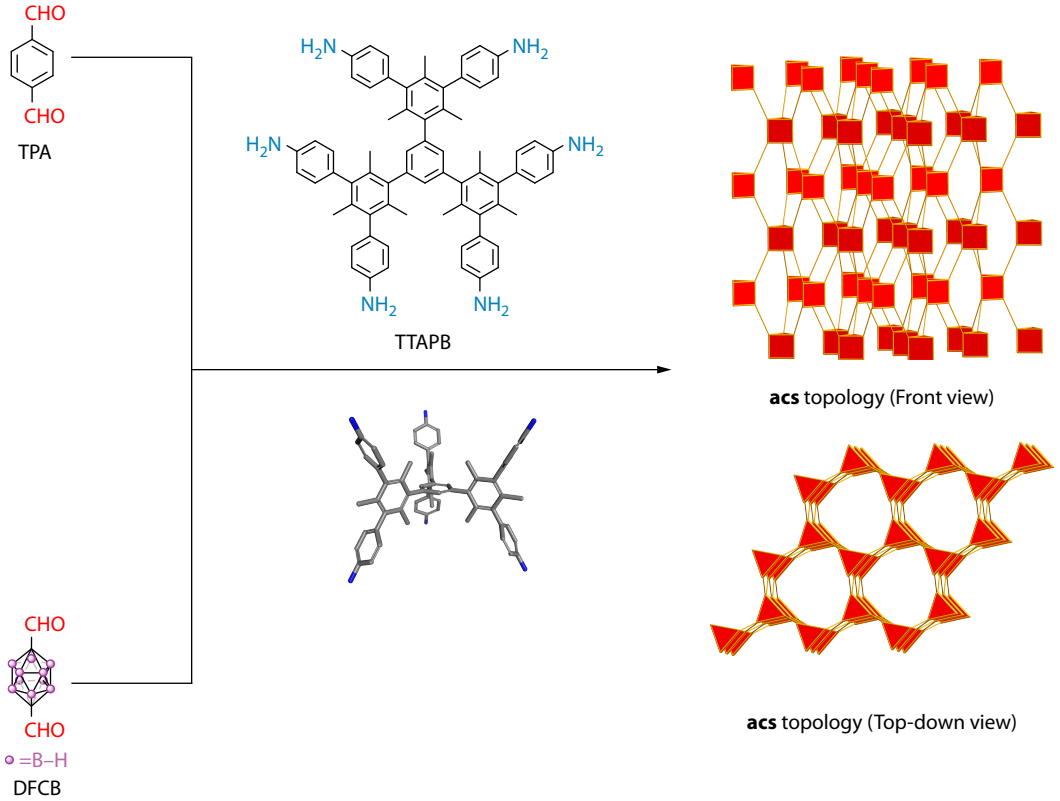

Fig. 1 Schematic diagrams for the synthesis of TTAPB-TPA-COF and TTAPB-DFCB-COF under solvothermal conditions.

https://doi.org/10.1007/s10118-026-3647-0

cm^{-1} for TTAPB-TPA-COF, confirming imine bond formation (Figs. S1 and S2 in ESI). Concurrently, the disappearance of the C=O stretches near 1750 and 1700 cm^{-1} indicates complete consumption of the aldehyde groups. ^{13}C CP-MAS NMR spectroscopy further verified the chemical composition: the imine carbon signal appeared at δ=153.9 ppm for TTAPB-DFCB-COF and δ=157.3 ppm for TTAPB-TPA-COF. Resonances at δ=18.1 ppm and δ=17.7 ppm were assigned to the methyl carbons in the respective frameworks, while a unique signal at δ=81.1 ppm in TTAPB-DFCB-COF corresponds to the carborane cage carbon atoms. The remaining peaks in both spectra were attributed to the aromatic carbons of the TTAPB node (Figs. S3 and S4 in ESI). TGA indicated a high thermal stability for both COFs up to 400 °C (Figs. S5 and S6 in ESI). The FE-SEM images revealed uniform, round cake-like morphologies for both materials (Figs. S7 and S8 in ESI), and EDS analysis confirmed the homogeneous distribution of key elements throughout the particles (Figs. S9 and S10 in ESI). The elemental analysis results for the C, H, and N contents were in excellent agreement with the theoretical values (Table S1 in ESI).

The crystal structures were determined by combining PXRD and computational modeling. The PXRD pattern of TTAPB-DFCB-COF exhibited distinct peaks at 4.45°, 4.91°, 7.46°, 8.93°, 10.48°, 12.08°, 17.31°, 18.27°, and 21.84° (Fig. 2a), while TTAPB-TPA-COF showed peaks at 4.55°, 6.10°, 7.61°, 9.10°, 10.57°, 12.15°, 13.97°, 17.51°, 18.32°, 18.89°, 21.73°, and 22.14° (Fig. 2b). After evaluating potential interpenetration configurations and symmetry options using Materials Studio, TTAPB-DFCB-COF and TTAPB-TPA-COF were identified as 2-fold and 6-fold interpenetrated **acs** networks, respectively (Figs. 2a and 2b, Fig. S11, Tables S2 and S3 in ESI). Pawley refinement supported these assignments, yielding lattice parameters of α=β=90°, γ=120°, a=b=36.7453 Å, c=41.8072 Å for TTAPB-DFCB-COF, and α=β=90°, γ=120°, a=b=16.5993 Å, c=39.9698 Å for TTAPB-TPA-COF. The close match between the experimental and simulated patterns is reflected in the low reliability factors (R_{wp}=2.35% and R_p=1.79% for TTAPB-DFCB-COF; R_{wp}=4.92% and R_p=3.75% for TTAPB-TPA-COF). The diffraction peaks of TTAPB-DFCB-COF are assigned to the (002), (2$\bar{1}$0), (3$\bar{2}$1), (031), (131), (2$\bar{2}$5), (062), (7$\bar{4}$3), and (451) planes (Fig. 2a). For TTAPB-TPA-COF, the peaks were indexed to (002), (100), (102), (004), (110), (200), (114), (213), (300), (302), (222), and (311) (Fig. 2b). These well-defined PXRD pro-

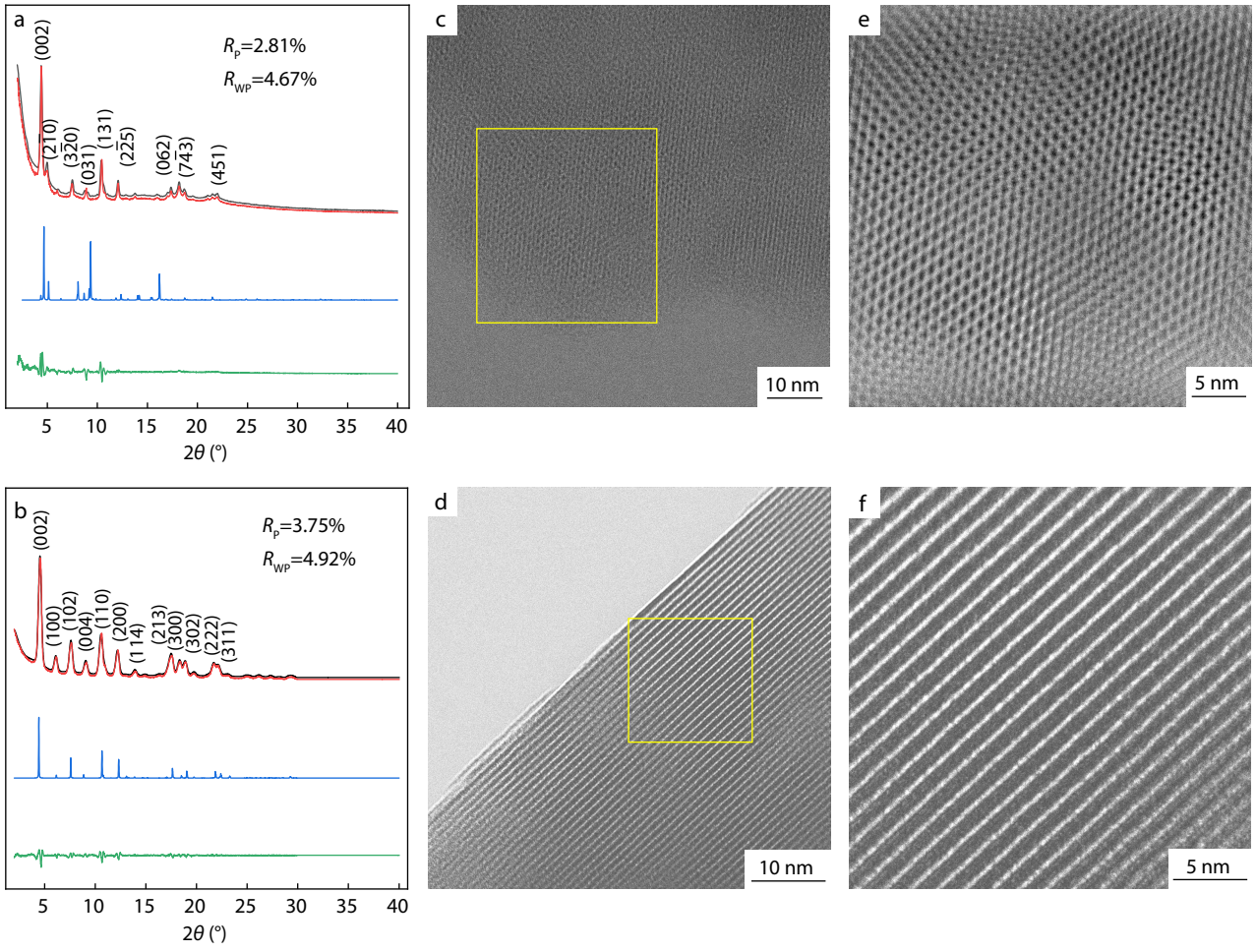

Fig. 2 PXRD patterns of (a) TTAPB-DFCB-COF and (b) TTAPB-TPA-COF (black curve, Pawley refined profile; red curve, experimental profile; blue curve, simulated profile; green curve, difference profile). HR-TEM images of (c) TTAPB-DFCB-COF and (d) TTAPB-TPA-COF. Enlarged inverse fast Fourier transform image of (e) TTAPB-DFCB-COF and (f) TTAPB-TPA-COF.

https://doi.org/10.1007/s10118-026-3647-0

files confirmed the highly ordered three-dimensional periodic structures of both COFs.

High-resolution transmission electron microscopy (HR-TEM) images provided further evidence of high crystallinity. The TTAPB-DFCB-COF exhibited a discernible periodic pore structure with a lower degree of interpenetration. In contrast, the highly interpenetrated TTAPB-TPA-COF exhibited distinct lattice fringes with a spacing of about 1.0 nm (Figs. 2c–2f). The structural divergence originates from the linker cores: the planar π-conjugated TPA linker favors dense packing and multidirectional $\pi\cdots\pi$ interactions, thermodynamically stabilizing the 6-fold interpenetrated architecture of TTAPB-TPA-COF. Conversely, the three-dimensional, electron-deficient carborane linker imposes pronounced steric constraints and directional $B^{\delta+}$–$H^{\delta-}\cdots\pi$ interactions that restrict network replication, resulting in a more open 2-fold interpenetrated framework of TTAPB-DFCB-COF framework. Collectively, the characterization data confirmed the successful synthesis of highly crystalline COFs with the expected structural integrity, providing a reliable foundation for the subsequent investigation of their pore microenvironments.

The design principle of this work originates from a fundamental comparison between two chemically distinct linker cores: the classic planar benzene and the three-dimensional aromatic carborane cluster. Despite the comparable molecular dimensions and similar kinetic diameters of about 0.54 nm (Fig. S12 in ESI), these units differ significantly in their molecular geometries and intermolecular interaction profiles. Benzene is characterized by a two-dimensional, π-conjugated aromatic system, which yields a relatively uniform electrostatic potential surface and facilitates multidirectional, diffuse $\pi\cdots\pi$ or C—H$\cdots\pi$ stacking as the primary driving force for molecular assembly.[48–50] In contrast, the carborane cluster is an electron-deficient, σ-aromatic icosahedron. Its most distinguishing features are a rigid, globular three-dimensional shape and highly polar B—H bonds, which generate localized regions of positive electrostatic potential ($B^{\delta+}$–$H^{\delta-}$). Consequently, the intermolecular forces governing carborane packing shift toward more directional and specific interactions, such as $B^{\delta+}$—$H^{\delta-}\cdots B^{\delta-}$—$H^{\delta+}$ contacts and $B^{\delta+}$–$H^{\delta-}\cdots\pi$ interactions with arene systems. An Independent Gradient Model based on Hirshfeld partition (IGMH) analyses visually confirmed that while benzene-benzene, carborane-benzene, and carborane-arborane interactions are van der Waals in nature, carborane-involved pairs exhibit weaker overall binding energies and pronounced orientational dependence, requiring an approach along the B—H bond axes for optimal electron overlap (Fig. 3).

The porosities of TTAPB-DFCB-COF and TTAPB-TPA-COF were first evaluated using nitrogen sorption isotherms at 77 K. Both materials exhibited nearly identical reversible type-I isotherms with sharp uptakes at low relative pressures (P/P_0), which are characteristic of microporous materials (Figs. 4a and 4b). Brunauer-Emmett-Teller (BET) surface areas and pore volumes, derived from adsorption data in the range $0.05 < P/P_0 < 0.30$, were 874 $m^2\cdot g^{-1}$ and 0.62 $cm^3\cdot g^{-1}$ for TTAPB-DFCB-COF, and 953 $m^2\cdot g^{-1}$ and 0.52 $cm^3\cdot g^{-1}$ for TTAPB-TPA-COF (Figs. 4a and 4b, Figs. S14 and S15 in ESI). Nonlocal density functional theory (NLDFT) calculations yielded pore sizes of 0.98 and 0.96 nm for TTAPB-DFCB-COF and TTAPB-TPA-COF, respectively (Figs. S13 and S14 in ESI), consistent with their theoretical values. Despite the similar adsorption properties observed in N_2 physisorption, the intrinsic differences in linker geometry, electronic structure, and degree of interpenetration fundamentally alter the pore architecture, most notably in terms of pore accessibility and chemical nature of the pore walls (Figs. 4c and 4d). To probe these subtle but critical variations in the pore microenvironment, we employed CO_2, CH_4, and N_2 as the molecular probes. These gases possess similar kinetic diameters (about 3.3–3.8 Å) but differ markedly in polarizability, dipole moment, and quadrupole moment (Table S4 in ESI), thereby serving as sensitive reporters of pore acces-

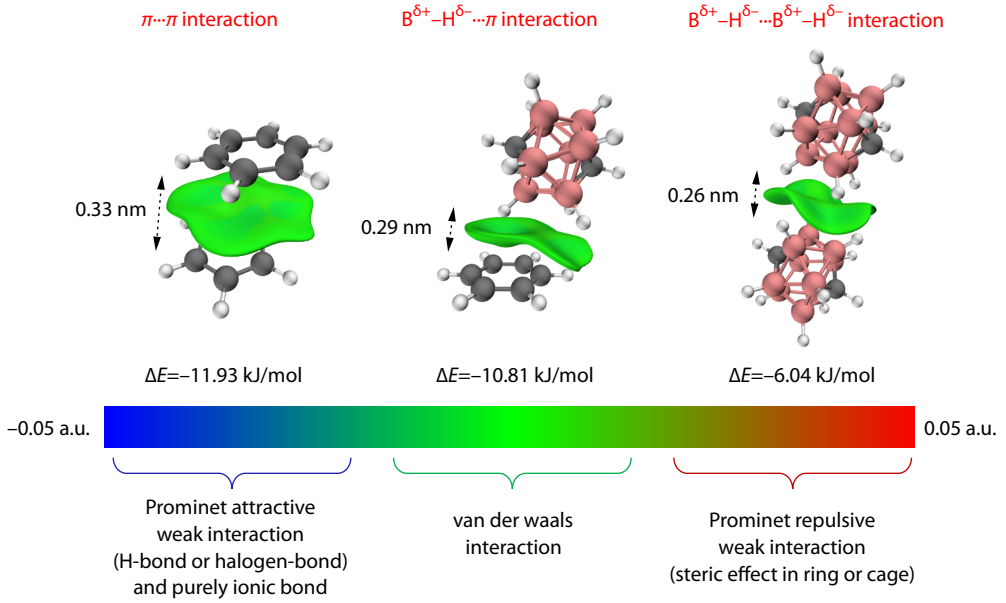

Fig. 3 IGMH analysis for the intermolecular interactions of benzene-benzene, carborane-benzene, and carborane-carborane, including their equilibrium distances and binding energies.

sibility, surface polarity, and specific host-guest interactions.

To visually illustrate the impact of differences in monomer composition and interpenetration architecture on pore functionality, we evaluated the single-component gas adsorption and isosteric heat of adsorption (Q_{st}) for CO_2, CH_4, and N_2 on 3D COFs at 273 and 298 K (Figs. 5a–5f, Fig. S15 in ESI). The adsorption capacity of TTAPB-TPA-COF for all gases exceeded that of TTAPB-DFCB-COF (Fig. 5a). This difference is attributed to their distinct interpenetration topologies. Although both frameworks share the same **acs** net topology and exhibit nearly identical pore sizes and BET surface areas, TTAPB-TPA-COF adopts a 6-fold interpenetrated architecture. This denser packing creates a more confined pore environment than the more open 2-fold interpenetrated structure of TTAPB-DFCB-COF, thereby enhancing the uptake of guest molecules. Notably, at 273 K and 0.1 MPa, TTAPB-TPA-COF adsorbed 33.9 cm^3/g of CH_4. The corresponding CH_4 uptake normalized to its BET surface area reached a relatively high value of 3.56×10^{-5} m^3/m^2, indicating promising potential for methane storage applications (Table S5 in ESI). In contrast, TTAPB-DFCB-COF exhibited higher selectivity for CO_2/N_2 and CO_2/CH_4 mixtures (Figs. 5d and 5e, Figs. S16–S21 in ESI). This enhanced selectivity likely originates from the specific $B^{\delta+}—H^{\delta-}\cdots C^{\delta+}=O^{\delta-}$ interaction between the polar B—H bonds in the carborane linker and the CO_2 molecules. Although CO_2, CH_4, and N_2 are all nonpolar (dipole moment

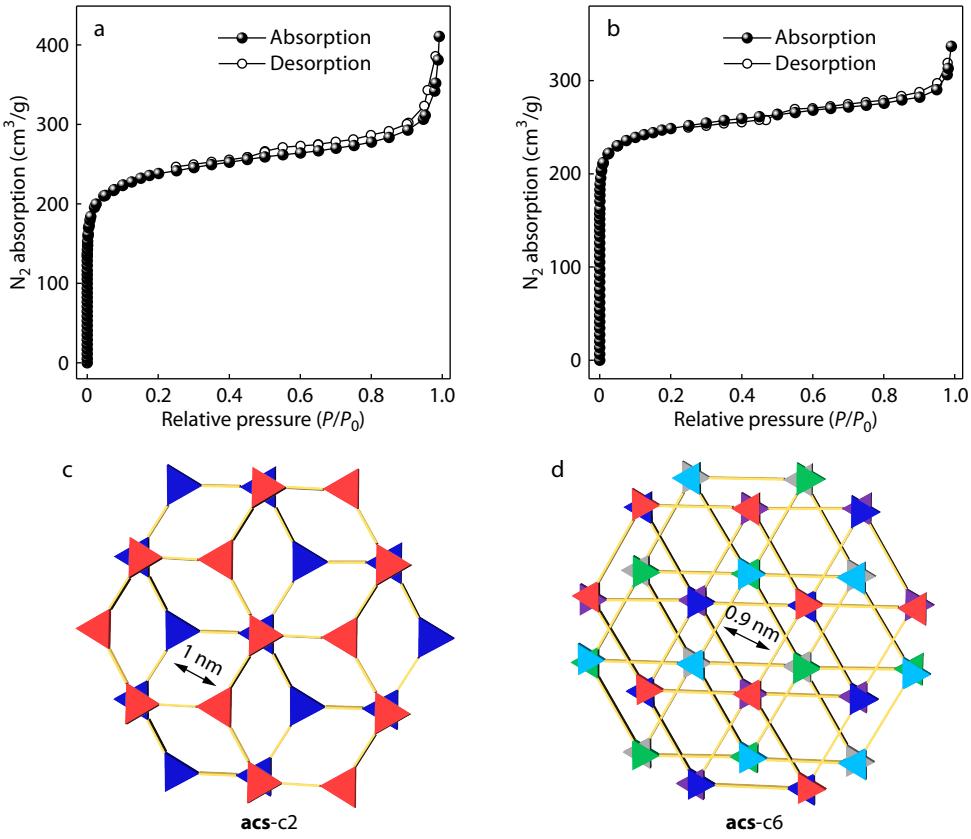

Fig. 4 Nitrogen sorption isotherms of (a) TTAPB-DFCB-COF and (b) TTAPB-TPA-COF. The crystal structures and corresponding acs topology with 2-fold for (c) TTAPB-DFCB-COF and 6-fold for (d) TTAPB-TPA-COF.

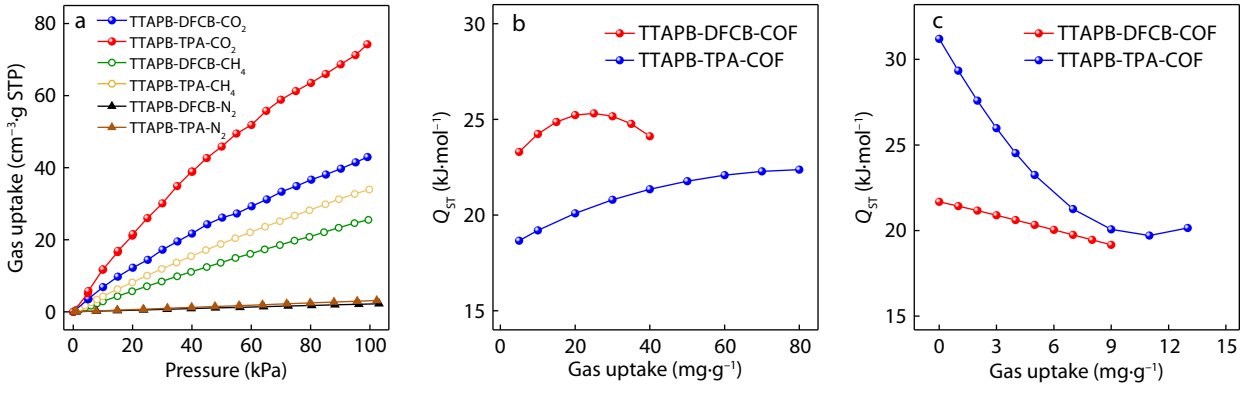

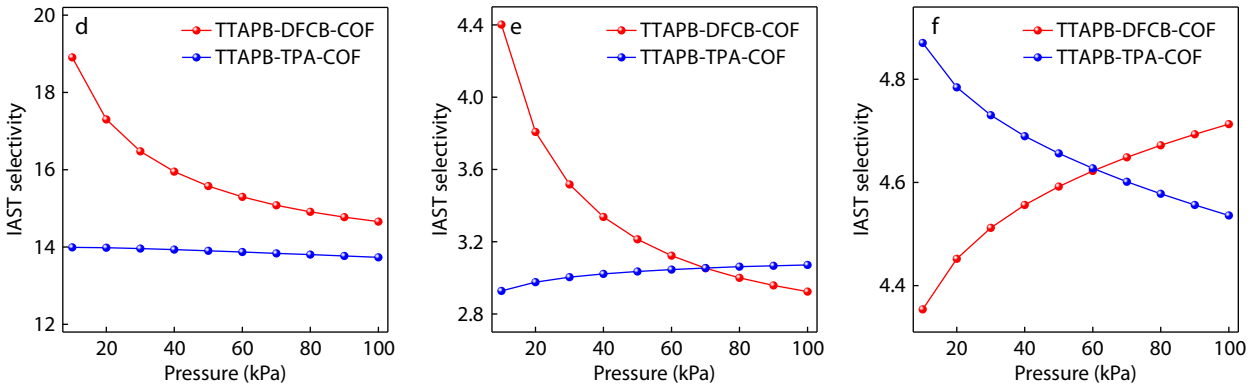

Fig. 5 (a) Three gas adsorption isotherms of TTAPB-DFCB-COF (blue for CO_2, green for CH_4 and black for N_2), and TTAPB-TPA-COF (red for CO_2, yellow for CH_4 and brown for N_2) at 273 K. Q_{st} for (b) CO_2 and (c) CH_4 of TTAPB-DFCB-COF (red curve) and TTAPB-TPA-COF (blue curve). IAST selectivity of (d) CO_2/N_2 (15/85, *V*/*V*), (e) CO_2/CH_4 (15/85, *V*/*V*) and (f) CH_4/N_2 (1/1, *V*/*V*) for TTAPB-DFCB-COF (red curve) and TTAPB-TPA-COF (blue curve) at 298 K.

μ=0), CO_2 possesses a significant quadrupole moment, whereas those of N_2 and CH_4 are negligible. This allows CO_2 to engage in strong, specific interactions with polar surfaces, whereas the adsorption of N_2 and CH_4 remains predominantly nonspecific. For TTAPB-DFCB-COF, the pore walls lined with numerous polar B—H sites provide such a surface precisely, distinguishing its selectivity from that of TTAPB-TPA-COF. The higher initial Q_{st} for CO_2 on TTAPB-DFCB-COF further supported this mechanism (Fig. 5b, Figs. S22 and S23 in ESI). At low pressures, the selectivity was governed primarily by the specific $B^{\delta+}—H^{\delta-}\cdots C^{\delta+}=O^{\delta-}$ interaction, resulting in the highest CO_2 selectivity. As the pressure increases, nonspecific van der Waals filling intensifies, increasing the relative uptake of N_2 or CH_4 and consequently reducing selectivity. In contrast, the weak nonspecific $\pi\cdots\pi$ interactions between TTAPB-TPA-COF and CO_2 showed little variation with pressure. Furthermore, TTAPB-TPA-COF exhibited higher CH_4/N_2 selectivity and a greater Q_{st} for CH_4 in most cases (Figs. 5c and 5f, Figs. S24 and S25 in ESI). This can be attributed to its ability to form stronger C—H$\cdots\pi$ interactions with CH_4 molecules, whereas neither COF exhibits significant specific interactions with N_2. These interactions not only contribute to its considerable CH_4 uptake, but also result in a high Q_{st} for CH_4 (31.2 kJ/mol), which ranks among the highest values reported for COFs at the time of this study (Fig. S26 in ESI).

CONCLUSIONS

In summary, this study establishes that the spatial geometry and electronic nature of the linear linker play a decisive role in governing the degree of interpenetration in 3D COFs. Using a sterically extended, 6-connected trigonal prismatic node (TTAPB) in combination with two structurally analogous but geometrically distinct linkers, planar terephthalaldehyde (TPA) and globular *C*,*C*-diformyl-*p*-carborane (DFCB), we synthesized an isoreticular pair of **acs**-topology COFs. Structural analysis revealed that the π-conjugated planar TPA linker facilitates dense packing, leading to a 6-fold interpenetrated framework (TTAPB-TPA-COF). In contrast, the bulky electron-deficient carborane linker in DFCB imposes steric and electronic constraints, resulting in a more open 2-fold interpenetrated architecture (TTAPB-DFCB-COF). This structural divergence directly dictates their contrasting gas-adsorption profiles: the narrower pores of the 6-fold interpenetrated TTAPB-TPA-COF yield higher gas-uptake capacities, whereas the polar pore surface of the 2-fold interpenetrated TTAPB-DFCB-COF, rich in B—H bonds, confers enhanced selectivity for CO_2 over N_2 and CH_4 through specific dipole-quadrupole interactions. These findings establish a clear structure-property relationship and demonstrate that the rational design of monomers, balancing geometry, steric demand, and electronic properties enables precise control over framework interpenetration. In turn, this control provides a powerful strategy for tailoring the pore environment and optimizing the functional performance of 3D COFs for advanced separation applications.

Conflict of Interests

The authors declare no interest conflict.

Electronic Supplementary Information

Electronic supplementary information (ESI) is available free of charge in the online version of this article at http://doi.org/10.1007/s10118-026-3647-0.

Data Availability Statement

The related data for this paper are available in the Science Data Bank (ScienceDB) database at (https://doi.org/10.57760/sciencedb.j00189.00046).

ACKNOWLEDGMENTS

This work was financially supported by the National Key R&D Program of China (No. 2022YFE0130700), the National Natural Science Foundation of China (No. 22375173), the China Postdoctoral Science Foundation (No. 2025M780159), and Postdoctoral Fellowship Program of CPSF (No. GZB20250042). The authors thank Shenghai Chang at the Center of Cyro-Electron Microscopy (CCEM), Zhejiang University, for his technical assistance with the Cyro-TEM.

REFERENCES

1 Diercks, C. S.; Yaghi, O. M. The atom, the molecule, and the covalent organic framework. *Science.* **2017**, *355*, eaal1585.
2 Geng, K. Y.; He, T.; Liu, R. Y.; Dalapati, S.; Tan, K. T.; Li, Z. P.; Tao, S. S.; Gong, Y. F.; Jiang, Q. H.; Jiang, D. L. Covalent organic frameworks: design, synthesis, and functions. *Chem. Rev.* **2020**, *120*, 8814–8933.
3 Li, Y. S.; Chen, W. B.; Xing, G. L.; Jiang, D. L.; Chen, L. New synthetic strategies toward covalent organic frameworks. *Chem. Soc. Rev.* **2020**, *49*, 2852–2868.
4 Waller, P. J.; Gándara, F.; Yaghi, O. M. Chemistry of covalent organic frameworks. *Acc. Chem. Res.* **2015**, *48*, 3053–3063.
5 Geng, K. Y.; Arumugam, V.; Xu, H. J.; Gao, Y. N.; Jiang, D. L. Covalent organic frameworks: Polymer chemistry and functional design. *Prog. Polym. Sci.* **2020**, *108*, 101288.
6 Xu, X. Y.; Huang, N. Multicomponent covalent organic frameworks: design strategies and synergistic functions. *Chem. Sci.* **2025**, *16*, 17034–17057.
7 Ma, T. Q.; Li, J.; Niu, J.; Zhang, L.; Etman, A. S.; Lin, C.; Shi, D. E.; Chen, P. H.; Li, H.; Du, X.; Sun, J. L.; Wang, W. Observation of interpenetration isomerism in covalent organic frameworks. *J. Am. Chem. Soc.* **2018**, *140*, 6763–6766.
8 Guan, X. Y.; Fang, Q. R.; Yan, Y. S.; Qiu, S. L. Functional regulation and stability engineering of three-dimensional covalent organic frameworks. *Acc. Chem. Res.* **2022**, *55*, 1912–1927.
9 Wang, H.; Yi, L. Z.; Hu, G. L.; Zhou, X.; Deng, H. X. Rigidity reinforcement of 3D covalent organic frameworks by controlling interpenetration. *J. Am. Chem. Soc.* **2025**, *147*, 9067–9073.
10 Furukawa, H.; Yaghi, O. M. Storage of hydrogen, methane, and carbon dioxide in highly porous covalent organic frameworks for clean energy applications. *J. Am. Chem. Soc.* **2009**, *131*, 8875–8883.
11 Li, Z. L.; Sheng, L.; Hsueh, C.; Wang, X. L.; Cui, H.; Gao, H. Q.; Wu, Y. Z.; Wang, J. L.; Tang, Y. P.; Xu, H.; He, X. M. Three-dimensional covalent organic frameworks with hea topology. *Chem. Mater.* **2021**, *33*, 9618–9623.
12 Yin, Y.; Zhang, Y.; Zhou, X.; Gui, B.; Wang, W. Q.; Jiang, W. T.; Zhang, Y. B.; Sun, J. L.; Wang, C. Ultra–highsurface area covalent organic frameworks for methane adsorption. *Science.* **2024**, *386*, 693–696.
13 Yang, L. T.; Cai, P. Y.; Jin, X. C.; Wang, Z. J.; Zhou, H. C.; Huang, N. Phenolic resin-type microporous organic polymers for high-performance carbon dioxide adsorption. *Chem Asian J.* **2025**, *20*, e202401288.
14 Han, X.; Huang, J. J.; Yuan, C.; Liu, Y.; Cui, Y. Chiral 3D covalent organic frameworks for high performance liquid chromatographic enantioseparation. *J. Am. Chem. Soc.* **2018**, *140*, 892–895.
15 Xu, X. Y.; Wu, X. Y.; Xu, K.; Xu, H.; Chen, H. Z.; Huang, N. Pore partition in two-dimensional covalent organic frameworks. *Nat. Commun.* **2023**, *14*, 3360.
16 Xu, X. Y.; Chen, H. Z.; Huang, N. Perylene-based 2D covalent organic frameworks for selective adsorption and extraction of

Graphical Abstract

Managing Interpenetration in 3D Covalent Organic Frameworks with Spatial-aromatic Building Blocks

Zhen-Yang Hu, Fu-Xiang Wen, Xiao-Yi Xu, and Ning Huang

Zhejiang University

Using a 6-connected triangular prismatic amine building block, an isoreticular pair of 3D COFs with **acs** topology was synthesized. The COF constructed from a planar-aromatic aldehyde building block exhibited a lower degree of interpenetration (2-fold) compared to its counterpart derived from a spatial-aromatic aldehyde building block (6-fold).

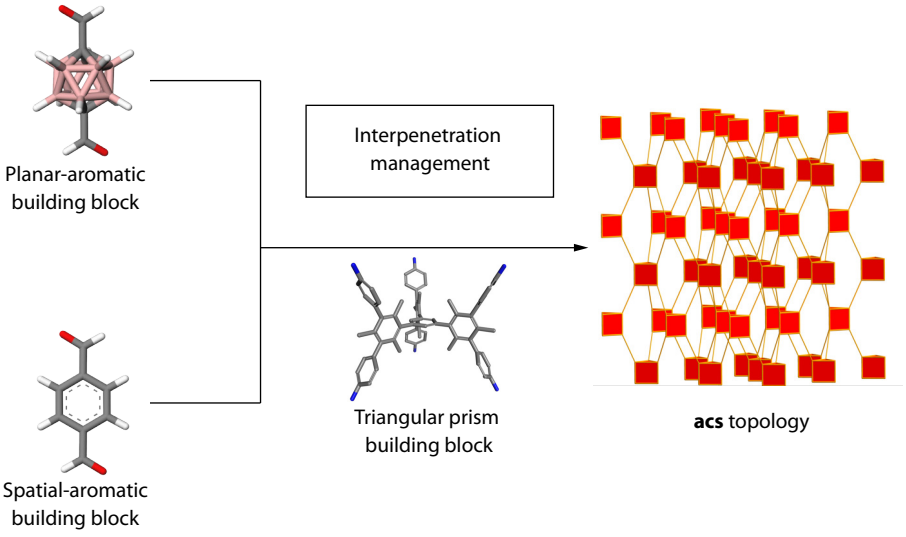

Chinese J. Polym. Sci. 2026, 44, 2395–2402 *https://doi.org/10.1007/s10118-026-3647-0*

C60. *Macromolecules* **2024**, *57*, 9457–9465.
17 Wu, T.; Qian, Y. J.; Zhu, Z. B.; Yu, W. H.; Zhang, L. F.; Liu, J.; Shen, X. W.; Zhou, X.; Qian, T.; Yan, C. L. Imine-linked 3D covalent organic framework membrane featuring highly charged sub-1 nm channels for exceptional lithium-ion sieving. *Adv. Mater.* **2025**, *37*, 2415509.
18 Wu, X. Y.; Zong, L. N.; Huang, N. Highly luminescent olefin-linked covalent organic frameworks. *Chem. Commun.* **2024**, *60*, 320–323.
19 Xu, K.; Feng, Y. Q.; Wen, F. X.; Xu, X. Y.; Wang, H. W.; Shui, Q. J.; Huang N. Topological control over porphyrin-based covalent organic frameworks for elucidating electron transfer characteristics. *Angew. Chem. Int. Ed.* **2025**, *64*, e202506977.
20 Feng, Y. Q.; Xu, X. Y.; Xu, K.; Huang N. Two-dimensional semiconducting covalent organic frameworks with unidirectional fused-ring bands. *J. Am. Chem. Soc.* **2025**, *147*, 41965–41972.
21 Srivastava, A. P.; Pandey, B. K. DFT-based evaluation of covalent organic frameworks for adsorption, optoelectronic, clean energy storage, and gas sensor applications. *J. Mol. Model.* **2025**, *31*, 302.
22 Hasija, V.; Patial, S.; Raizada, P.; Khan, A. A. P.; Asiri, A. M.; Le, V. Q.; Nguyen, V. H.; Singh, P. Covalent organic frameworks promoted single metal atom catalysis: strategies and applications. *Coord. Chem. Rev.* **2022**, *452*, 214298.
23 Wen, F. X.; Xu, K.; Feng, Y. Q.; Huang N. Two-dimensional covalent organic frameworks with pentagonal pores. *J. Am. Chem. Soc.* **2024**, *146*, 19680–19685.
24 Niu, S.; Hu, Z. Y.; Xu, X. Y.; Xiong, Z. P.; Chen, H. Z.; Jen, A. K. -Y.; Huang N. Structural regulation of three-dimensional covalent organic frameworks for efficient photoredox catalysis toward atom transfer radical polymerization. *Angew. Chem. Int. Ed.* **2025**, *64*, e202424860.
25 Yue, Y.; Ren, R.; He, Q. G.; Wang, G. J.; Chen, H. Z.; Huang, N. Checkerboard-like bimetallic covalent organic frameworks as efficient electrocatalysts for oxygen reduction reaction. *ACS Appl. Mater. Interfaces* **2025**, *17*, 35950–35957.
26 Feng, Y. Q.; Huang, N. Porphyrin and phthalocyanine-based covalent organic frameworks for electrocatalytic CO_2 reduction: from structural design to future perspectives. *Green Chem.* **2025**, *27*, 15002–15023.
27 Das, S.; Sekine, T.; Mabuchi, H.; Irie, T.; Sakai, J.; Zhao, Y.; Fang, Q. R.; Negishi, Y. Three-dimensional covalent organic framework with scu-c topology for drug delivery. *ACS Appl. Mater. Interfaces* **2022**, *14*, 48045–48051.
28 Ghosh, P.; Banerjee, P. Drug delivery using biocompatible covalent organic frameworks (COFs) towards a therapeutic approach. *Chem. Commun.* **2023**, *59*, 12527–12547.
29 Shi, Y. Q.; Yang, J. L.; Gao, F.; Zhang, Q. H. Covalent organic frameworks: recent progress in biomedical applications. *ACS Nano.* **2023**, *17*, 1879–1905.
30 Mehvari, F.; Ramezanzade, V.; Asadi, P.; Singh, N.; Kim, J.; Dinari, M.; Kim, J. S. A panoramic perspective of recent progress in 2D and 3D covalent organic frameworks for drug delivery. *Aggregate* **2024**, *5*, e480.
31 Liu, Y. M.; Wu, C. Y.; Sun, Q. Z.; Hu, F.; Pan, Q. Y.; Sun, J.; Jin, Y. H.; Li, Z. B.; Zhang, W.; Zhao, Y. J. Spirobifluorene-based three-dimensional covalent organic frameworks with rigid topological channels as efficient heterogeneous catalyst. *CCS Chem.* **2020**, *3*, 2418–2427.
32 Sun, Q. Z.; Wu, C. Y.; Pan, Q. Y.; Zhang, B. J.; Liu, Y. M.; Lu, X. Y.; Sun, J.; Sun, L. S.; Zhao, Y. J. Three-dimensional covalent-organic frameworks loaded with highly dispersed ultrafine palladium nanoparticles as efficient heterogeneous catalyst. *ChemNanoMat* **2021**, *7*, 95–99.
33 Yu, B. Q.; Li, W. L.; Wang, X.; Li, J. H.; Lin, R. B.; Wang, H. L.; Ding, X.; Jin, Y. C.; Yang, X. Y.; Wu, H.; Zhou, W.; Zhang, J. P.; Jiang, J. Z. Observation of interpenetrated topology isomerism for covalent organic frameworks with atom-resolution single crystal structures. *J. Am. Chem. Soc.* **2023**, *145*, 25332–25340.
34 Yu, B. Q.; Tao, Y.; Yao, X.; Jin, Y. C.; Liu, S.; Xu, T. T.; Wang, H. L.; Wu, H.; Zhou, W.; Zhou, X.; Ding, X.; Wang, X.; Xiao, X.; Zhang, Y. B.; Jiang, J. Z. Single-crystalline 3D covalent organic frameworks with exceptionally high specific surface areas and gas storage capacities. *J. Am. Chem. Soc.* **2024**, *146*, 28932–28940.
35 Wang, K. X.; Li, Z. P.; Chen, X. Y.; Cui, Y. Synthesis, structure and characterization of a dihydrophenazine based 3D covalent organic framework. *Chem. J. Chin. Univ.* **2022**, *43*, 133–139.
36 Maiti, S.; Tan, K.; Geng, S. B.; Gupta, A. K.; VanNatta, P. E.; Yuan, D. Q.; Zhang, Z. J.; Verma, G.; AlShahrani, T.; Ma, S. Q. Interpenetrated three-dimensional covalent organic framework for selective adsorption of C_2H_2 over CO_2 and C_2H_4. *Macromol. Rapid Commun.* **2025**, *46*, e00317.
37 Wang, Y. J.; Liu, Y. Z.; Li, H.; Guan, X. Y.; Xue, M.; Yan, Y. S.; Valtchev, V.; Qiu, S. L.; Fang, Q. R. Three-dimensional mesoporous covalent organic frameworks through steric hindrance engineering. *J. Am. Chem. Soc.* **2020**, *142*, 3736–3741.
38 Wang, K. X.; Hou, B.; Dong, J. Q.; Niu, H. L.; Liu, Y.; Cui, Y. Controlling the degree of interpenetration in chiral three-dimensional covalent organic frameworks via steric tuning. *J. Am. Chem. Soc.* **2024**, *146*, 21466–21475.
39 Núñez, R.; Romero, I.; Teixidor, F.; Viñas, C. Icosahedral boron clusters: a perfect tool for the enhancement of polymer features. *Chem. Soc. Rev.* **2016**, *45*, 5147–5173.
40 Núñez, R.; Tarrés, M.; Ferrer-Ugalde, A.; de Biani, F. F.; Teixidor, F. Electrochemistry and photoluminescence of icosahedral carboranes, boranes, metallacarboranes, and their derivatives. *Chem. Rev.* **2016**, *116*, 14307–14378.
41 Štíbr, B. Recent aspects of the ten-vertex dicarbaborane chemistry. *J. Organomet. Chem.* **2018**, *865*, 4–11.
42 Marfavi, A.; Kavianpour, P.; Rendina, L. M. Carboranes in drug discovery, chemical biology and molecular imaging. *Nat. Rev. Chem.* **2022**, *6*, 486–504.
43 Meng, Y. X.; Lin, X.; Huang, J. Y.; Zhang, L. L. Recent advances in carborane-based crystalline porous materials. *Molecules* **2024**, *29*, 3916.
44 Zhang, X.Y.; Rendina, L. M.; Müllner, M. Carborane-containing polymers: synthesis, properties, and applications. *ACS Polym. Au.* **2024**, *4*, 7–33.
45 Xu, X. Y.; Cui, Q. R.; Chen, H. Z.; Huang, N. Carborane-based three-dimensional covalent organic frameworks. *J. Am. Chem. Soc.* **2023**, *145*, 24202–24209.
46 Zhu, Q.; Wang, X.; Clowes, R.; Cui, P.; Chen, L. J.; Little, M. A.; Cooper, A. I. 3D cage COFs: a dynamic three-dimensional covalent organic framework with high-connectivity organic cage nodes. *J. Am. Chem. Soc.* **2020**, *142*, 16842–16848.
47 Yin, Y.; Zhang, Y.; Zhou, X.; Gui, B.; Cai, G. H.; Sun, J. L.; Wang, C. Single-crystal three-dimensional covalent organic framework constructed from 6-connected triangular prism node. *J. Am. Chem. Soc.* **2023**, *145*, 22329–22334.
48 Lohse, M. S.; Rotter, J. M.; Margraf, J. T.; Werner, V.; Becker, M.; Herbert, S.; Knochel, P.; Clark, T.; Bein, T.; Medina, D. D. From benzodithiophene to diethoxy-benzodithiophene covalent organic frameworks – structural investigations. *CrystEngComm.* **2016**, *18*, 4295–4302.
49 Nguyen, V.; Grünwald, M. Microscopic origins of poor crystallinity in the synthesis of covalent organic framework COF-5. *J. Am. Chem. Soc.* **2018**, *140*, 3306–3311.
50 Pelkowski, C. E.; Natraj, A.; Malliakas, C. D.; Burke, D. W.; Bardot, M. I.; Wang, Z. X.; Li, H. Y.; Dichtel, W. R. Tuning crystallinity and stacking of two-dimensional covalent organic frameworks through side-chain interactions. *J. Am. Chem. Soc.* **2023**, *145*, 21798–21806.